

Advances in the Development of the Attitude Determination and Control System of the CubeSat MOVE-II

*D. Messmann¹, T. Gruebler¹, F. Coelho², T. Ohlenforst¹, J. van Bruegge¹,
F. Mauracher¹, M. Doetterl¹, S. Plamauer¹, P. Schnierle¹, T. Kale¹, M. Seifert¹, A. Fuhrmann¹,
E. Karagiannis¹, A. Ulanowski¹, T. Lausenhammer¹, A. Meraner¹, M. Langer¹*

¹*Institute of Astronautics, Technical University of Munich*

Boltzmannstrasse 15, 85748 Garching, Germany

²*Federal University of Santa Maria, Brazil*

Av. Roraima, 1000, Camobi 97105-900 Santa Maria, RS, Brazil

David Messmann david.messmann@tum.de · Thomas Gruebler thomas.gruebler@tum.de

Abstract

MOVE-II (Munich Orbital Verification Experiment) will be the first CubeSat of the Technical University of Munich (TUM) utilizing a magnetorquer-based active attitude determination and control system (ADCS). The ADCS consists of six circuit boards (five satellite side panels and one central circuit board in satellite stack), each equipped with a microcontroller, sensors and an integrated coil. The design enables redundancy and therefore forms a fault-tolerant system with respect to sensors and actuators. The paper describes the hardware implementation, algorithms, software architecture, and first test results of the integrated ADCS on the engineering unit. A possibility to upgrade and extend our software after launch will enable further research on new and innovative attitude determination and control strategies and distributed computation on satellites. The MOVE-II flight unit is in the integration and test phase with an intended launch date in early 2018.

1. Introduction

Owing to relatively low costs necessary for development and launch, and the opportunity to use commercial off-the-shelf (COTS) components, CubeSats¹ are being developed in universities and companies all over the world. They enable small payloads to get access to space and students to obtain hands-on experience about spacecraft technologies.² MOVE-II³ is a one Unit (1U) CubeSat ($10 \times 10 \times 10 \text{ cm}^3$), which is being developed by students at the Technical University of Munich (TUM). The project is a cooperation between the Institute of Astronautics (LRT) and the astronautical student research group Wissenschaftliche Arbeitsgemeinschaft für Raketentechnik und Raumfahrt (WARR) of TUM. The goal of the MOVE-II mission is to test, verify and qualify a new satellite bus for future mission with demanding scientific payloads, evolving the subsystems that were developed in-house for TUM's first CubeSat First-MOVE⁴ and applying the lessons learned⁵ from that project. As payload of MOVE-II, the performance and degradation of novel solar cells in outer space shall be investigated.⁶ The launch into a 575 km sun-synchronous orbit (SSO) is scheduled for early 2018. The assembled engineering model (EM) of MOVE-II is illustrated in Figure 1 and 2.

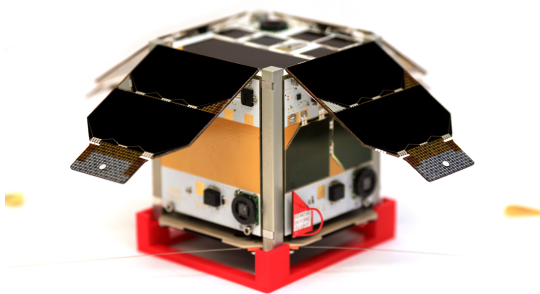


Figure 1: The assembled engineering model of the MOVE-II satellite

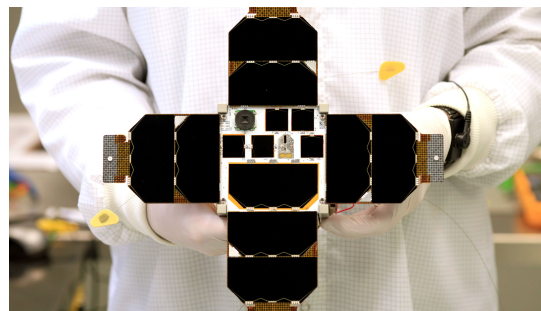


Figure 2: Top view of the assembled engineering model of the MOVE-II satellite

MOVE-II ADCS

As opposed to its predecessor mission First-MOVE, MOVE-II will be the first satellite of the LRT that features a magnetorquer-based active ADCS. The mission and payload of MOVE-II requires two different control modes: A B-Dot controller is implemented to reduce the initial angular velocities of the CubeSat after ejection from its deployer. After successful completion of the detumbling maneuver, the top side, featuring the payload and the solar cells of the satellite, is pointing towards the sun. The top view is illustrated in Figure 2. Sun pointing ensures enough power for the satellite while maintaining the orientation of the payload. The attitude of the satellite will be estimated by an Extended Kalman Filter (EKF) fusing sensor data from magnetic field sensors, gyroscopes and sun sensors. The ADCS hardware consists of six printed circuit boards (PCB) in total. This hardware design represents a control system with redundant actuators and sensors, and thus yields in a highly redundant and fault-tolerant ADCS, which enables continuity even with failures in the redundant control panels. The ADCS software can be upgraded and extended even after launch. This enables flexible and powerful research, which provides the possibility to investigate new and innovative attitude determination and control strategies once in orbit.

The upcoming sections give an insight into the development and design criteria of our ADCS. The paper is structured as follows: At the beginning the hardware architecture and components of the ADCS are described. Second, the attitude determination and control concept are introduced. Moreover, a test result for the detumbling control is shown. The third part of the paper presents the software architecture and features. Finally, a short conclusion is given.

2. Hardware

This section presents the design of the ADCS hardware including the magnetorquers and the sensors which are utilized for attitude estimation.

2.1 System Architecture

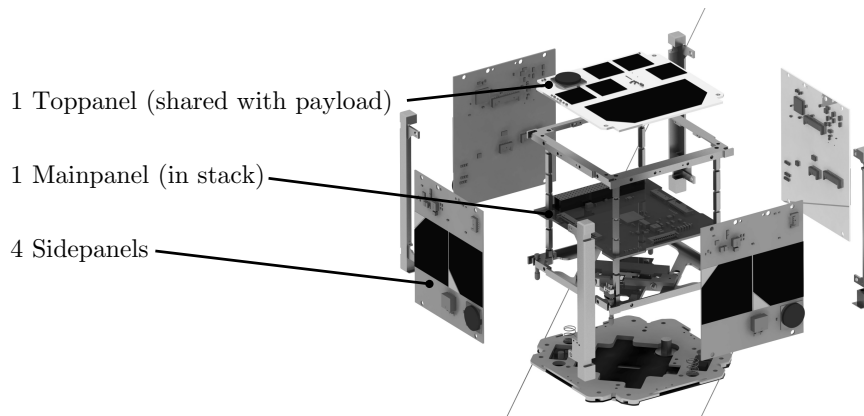


Figure 3: Distribution of ADCS panels on the MOVE-II CubeSat

Printed Circuit Board (PCB) integrated magnetorquer coils are constructed out of square shaped PCB traces directly inside the PCB. Such printed coils are robust and space-saving, allow stable manufacturing, and lower the integration time of the satellite. This makes printed coils a preferred choice as magnetorquers for the MOVE-II CubeSat. The coils are described in section 2.4.

To generate a magnetic field vector in any desired direction, at least three magnetorquer coils need to be mounted perpendicular to each other. As the inner side of the body is already largely occupied by other subsystems, we decided to use the PCBs with integrated coils as outer hull of the satellite. One board is located in the inner stack, as the S-band antenna occupies the bottom side of the satellite. The outer panels, called Sidepanels and Toppanel, are also used for solar cells and payload. Figure 3 shows the arrangement of all ADCS PCBs on the satellite. Additionally to the coils, each panel is also equipped with a dedicated coil driver, microcontroller and several attitude determination sensors. The ADCS mainboard, referred to as Mainpanel, forms the central, non-redundant element of the system. It is located in the board stack and connected to the rest of the satellite systems via a common PC/104 interface. The data exchange between the Mainpanel and the command and data handling system (CDH) of the satellite is realized via four-wire SPI. Also all the Sidepanels and the Toppanel are connected via SPI to the central Mainpanel.

All four Sidepanels and the Toppanel are electrically equal, therefore it is possible to run exactly the same software binaries on all five outer panels.

2.2 Electronic Architecture

Figure 4 depicts all major components and electrical connections between all panels. The Mainpanel is the central element of the system. The Sidepanels are connected over individual connectors to the Mainpanel, whereas the Toppanel utilizes some pins of the PC/104 connector exclusively.

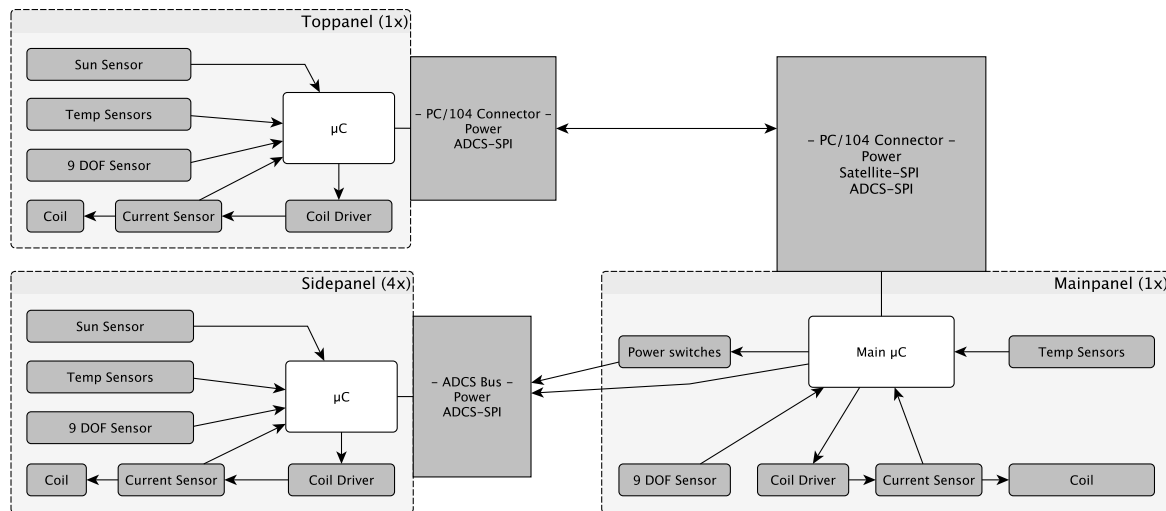


Figure 4: Overview of the detailed ADCS architecture. It consists of a Mainpanel, four Sidepanels and a Toppanel which is electrically equal to a Sidepanel. Each panel is equipped with a nine degree of freedom (9 DOF) sensor which consists of a three-axis magnetometer, a three-axis gyroscope, and a three-axis accelerometer (unused). The outer panels each feature one additional sun sensors.

The chosen microcontroller family on all panels is Atmel AVR XMega which was test flown on a sounding rocket experiment in 2014.⁷ It features direct memory access (DMA) between the panels and to the CDH to enable the necessary system performance. The outer panels feature a smaller Atmel ATxmega128A4U microcontroller utilizing 44 pins,⁸ whereas the Mainpanel integrates an ATxmega256A3U microcontroller utilizing 64 pins and a larger memory.⁹ The additional pins are used for interfacing the Sidepanels and the Toppanel. Additionally, the Mainpanels and Toppanels microcontroller Program and Debug Interface (PDI)¹⁰ is connected to the CDH to enable easy software upgrades. The Sidepanel microcontrollers PDI is connected to the Mainpanel for upgrading and reflashing the Sidepanels software.

The Sidepanels and the Toppanel are connected over two individual SPI buses to the Mainpanel. The panels are grouped in a way that if one bus fails (e.g. by electrical short circuit caused by one broken Sidepanel microcontroller), the system can still make use of all three working axes on the other bus to continue attitude determination and actuation. The only non-redundant loss in such a case would be two or three sun sensors of five available sensors. All other sensors are redundant (see section 2.3). All sensors on each panel are connected to the logically same microcontroller interface to enable exact double use of the needed driver code.

The coil integrated in each board and actuated through the coil driver is described in section 2.5. The actuation of all coils is set by the microcontroller of the Mainpanel, whereas each distributed microcontroller takes care of the current control of its own associated coil. An additional feature of the Mainpanel is the possibility to cut off the power of the five ADCS Panels. The switching circuits are constructed from discrete MOSFETs. The 3.3 V and 5 V power supply of the Panels can be switched separately to enable smart power saving, help on-orbit debugging, and allow isolation and disconnecting of potentially malfunctioning components.

2.3 Sensors

At least two non-parallel vector measurements are required to determine the absolute attitude.¹¹ The two distinct attitude vectors are obtained from the sun position sensor NANO-ISS60 by SolarMEMS and the three-axis magnetic

MOVE-II ADCS

field sensor BMX055 from Bosch Sensortec which is also equipped with a temperature sensor in it. The analog sun position sensor uses four photo diodes in a squared configuration which are covered by a pinhole. Depending on the incident angle of the sun, the photo diodes are partly illuminated. From the four analog output signals the sun vector can be calculated. The field of view is 120° . A sheet of $100\ \mu\text{m}$ thick CMX glass from Qioptiq is attached on the sensor to protect it from radiation damage caused by charged particles. The analog output of the sensor is additionally filtered by means of a simple, first-order RC lowpass with a 25 Hz cut-off frequency. The internal analog digital converter of the microcontroller measures the voltage with a 12 bit resolution.^{8,9}

The BMX055 features three independent sensor modules in one package: a three-axis magnetometer, three-axis gyroscope and three-axis accelerometer. The microcontroller receives the sensor data digitally via SPI. All control parameters such as the range, readout rate and the amount of values to average from, can be set within its software feature set.¹² The sensors are placed directly in the center of the panels to measure the magnetic field of each individual coil. Since each panel features a BMX055 sensor, the measurements are six-fold redundant. This allows us to disable most of the BMX055 for powersaving and switch to another sensor in case of a malfunction. The magnetometers, the sun sensors and the gyroscopes are utilized for attitude estimation (see section 3.1). The accelerometers are not employed for determining attitude. In addition to the introduced sensors, the panels are equipped with four temperature sensors each. The temperature sensors are placed in a way to allow later on-orbit debugging in case of hardware failures and are used by the Thermal subsystem to get an overall thermal view of the satellite. There are three Maxim Integrated 1-Wire DS18B20U sensors and another temperature sensor inside the BMX055. The 1-Wire sensors have a accuracy of 0.5°C in the the range from -10°C to 85°C and they are resistant to radiation.¹³

2.4 Coils

The satellite features six coils as magnetorquers. Five identical coils are integrated inside the four Sidepanels and the Toppanel, and a different coil in the Mainpanel. Figure 5 and 6 show a rendering of the coils. The coils extend over the six inner layers of the PCBs. The different designs are due to different structural constraints of the panels and the presence of electronics on the external PCB layers. The coil design parameters are optimized to minimize the power consumption of each coil. The Side- and Toppanel coils have a size of $65 \times 67\ \text{mm}^2$, comprising a total of 13 windings per layer with a track width of $988\ \mu\text{m}$ and thickness of $35\ \mu\text{m}$. The Mainpanel coil has a size of $65 \times 67\ \text{mm}^2$ with 15 windings per layer, having a track width of $1248\ \mu\text{m}$ and thickness of $35\ \mu\text{m}$. The optimal operation voltage is 1.5 V, generating a dipole moment of $0.05\ \text{A m}^2$ per coil at room temperature. The resulting $0.1\ \text{A m}^2$ dipole moment per axis is a value that has been targeted by other CubeSat missions,^{14–16} and has therefore been used as a reference for the coil design process. The power consumption for two Sidepanels at the targeted dipole moment is 0.76 W. This is only needed during detumbling and experimental maneuvers. The nominal power consumption will be much less, as we particularly focused on reducing all residual dipole moments on the whole satellite.

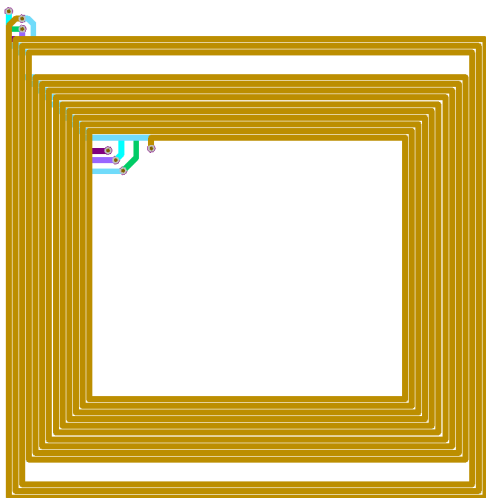


Figure 5: Rendering of the Side- and Toppanel coil

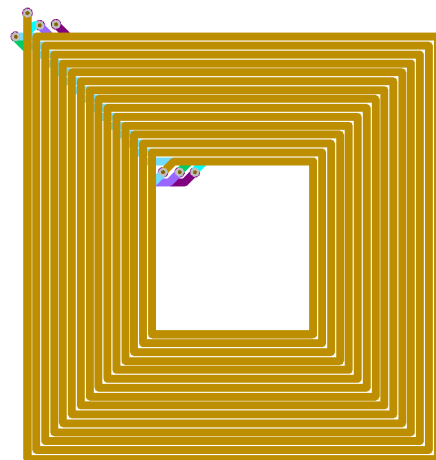


Figure 6: Rendering of the Mainpanel coil

2.5 Coil Driver

The coil driver is made of discrete components. Figure 7 gives an overview of the schematics. A first stage converts the 5 V input voltage to a constant current by means of a buck converter.¹⁷ The buck converter is operated with a 512 kHz pulse-width modulated (PWM) signal generated by the microcontroller. An additional sense resistor (Rload) enables active control of the coil current to compensate temperature dependencies. In a second stage, a H-bridge circuit enables to set the coil current direction.¹⁷

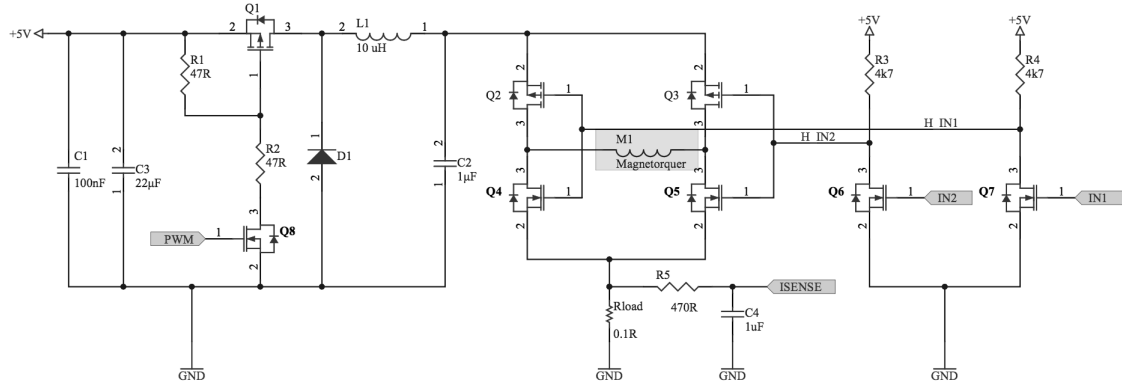


Figure 7: Schematics of the implemented coil driver. The left side (with main components Q1, D1, L1 and C2) forms the buck converter. The right side (Q2-5) forms the H-bridge. Rload is the sense resistor used for coil current measurement.

3. Attitude Determination Concept

Estimating attitude knowledge is required for advanced attitude control methods, which utilizes a state feedback.

3.1 Attitude Determination System Overview

MOVE-II facilitates an EKF for state estimation. Furthermore, the Singular Value Decomposition (SVD) method is implemented as a deterministic method, which is used for sanity check and initial state estimation. Referring to Vinter¹⁸ the SVD-method is a fast and robust method to solve Wahba's Problem.¹⁹ Using two different vector observations, the sun vector and the Earth's magnetic field vector, the attitude can be determined for one time instant. Attitude estimators need reference models and measurements as inputs. Since the magnetometer and the sun sensor provide a measurement, corresponding reference models have to be implemented to provide the vectors in a reference frame. The sun position model which is well described in Montenbruck²⁰ and the International Geomagnetic Reference Field 12 (IGRF 12²¹) for Earth's magnetic field calculation, are used. The IGRF 12 model requires the orbital position. A commonly used method to propagate an orbit is the Simplified General Perturbation 4 (SGP4, described in Hoots²²) model which has been implemented on several CubeSat missions.^{14, 16, 23} This orbit propagator requires a Two-Line Element (TLE) set and the Julian Date as inputs in order to obtain the position of the satellite in orbit. For the magnetic field model, Earth's rotation has to be taken into account. The model described in Jensen,¹⁴ was selected to be used. The implementation of the SGP4 and IGRF 12 is based on the work of Jensen.¹⁴

Alternatively, the GPS device, which is featured on the CDH board, can be used for position determination. However, the GPS sensor usage for the attitude determination concept is not intended in the primary mission phase. The GPS performance will be a research activity for investigation in space. The Figure 8 illustrates the architecture of the attitude determination system.

3.2 Extended Kalman Filter

An approach which estimates the attitude and the gyroscope bias is considered. Let the measured angular rate be given by the three-axis gyroscope model described as follows:^{11, 25}

$$\tilde{\omega} = \omega + \beta + \eta_v \quad (1)$$

$$\dot{\beta} = \eta_u \quad (2)$$

MOVE-II ADCS

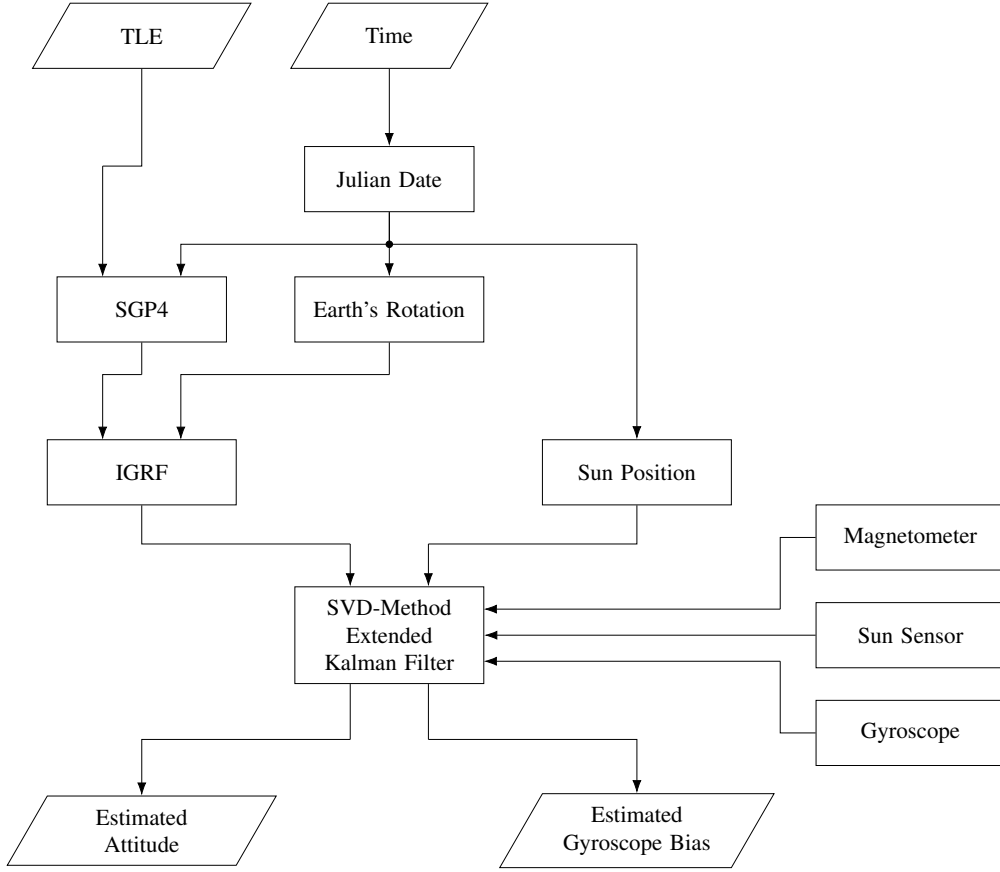


Figure 8: Flow diagram of the attitude determination system. Several models and sensors are used as an input for the attitude determination techniques EKF and SVD.

where $\tilde{\omega}$ is the measured angular rate vector, β is the bias in gyroscope measurements, and η_v and η_u are independent zero-mean Gaussian white-noise processes with spectral densities σ_v^2 and σ_u^2 , respectively. The propagation step in the filtering process predicts the next state of the system via kinematics model as function of the filtered gyroscope measurements computing:

$$\hat{\omega}_{k|k-1} = \tilde{\omega}_{k-1} - \hat{\beta}_{k-1} \quad (3)$$

$$\hat{q}_{k|k-1} = \left(I_{4 \times 4} + \frac{\Delta t}{2} \Omega(\hat{\omega}_{k|k-1}) \right) \hat{q}_{k-1|k-1} \quad (4)$$

$$P_{k|k-1} = \Phi_k P_{k-1|k-1} \Phi_k^T + \Gamma Q_k \Gamma^T \quad (5)$$

where $\hat{\omega}_{k|k-1} \in \mathbb{R}^3$, $\hat{q}_{k|k-1} \in \mathbb{R}^4$ and $P_{k|k-1} \in \mathbb{R}^{6 \times 6}$ refer to the propagated angular rate, the attitude quaternion and the state error covariance matrix, respectively, at time step k . Matrix $\Omega(\omega) \in \mathbb{R}^{4 \times 4}$ in (4) is defined as

$$\Omega(\omega) \equiv \begin{bmatrix} 0 & -\omega^T \\ \omega & [\omega \times]^T \end{bmatrix} \quad (6)$$

with $[\cdot \times]$ as the skew-symmetric operator and matrices $\Phi_k \in \mathbb{R}^{6 \times 6}$ and $\Gamma_k \in \mathbb{R}^{6 \times 6}$ in (5) are defined as

$$\Phi_k \equiv \begin{bmatrix} \Phi_{11} & \Phi_{12} \\ \mathbf{0}_{3 \times 3} & \mathbf{I}_{3 \times 3} \end{bmatrix} \quad (7)$$

$$\begin{aligned} \Phi_{11} &= \mathbf{I}_{3 \times 3} - \Delta t [\hat{\omega}_k \times] + \frac{\Delta t^2}{2} [\hat{\omega}_k \times]^2 \\ \Phi_{12} &= -\Delta t \mathbf{I}_{3 \times 3} + \frac{\Delta t}{2} [\hat{\omega}_k \times] - \frac{\Delta t^3}{6} [\hat{\omega}_k \times]^2 \end{aligned}$$

$$\Gamma_k \equiv \begin{bmatrix} -\mathbf{I}_{3 \times 3} & \mathbf{0}_{3 \times 3} \\ \mathbf{0}_{3 \times 3} & \mathbf{I}_{3 \times 3} \end{bmatrix} \quad (8)$$

The discrete process noise covariance $\mathbf{Q}_k \in \mathbb{R}^{6 \times 6}$ is computed as follows:

$$\mathbf{Q}_k \approx \begin{bmatrix} (\sigma_v^2 \Delta t + \frac{1}{3} \sigma_u^2 \Delta t^3) \mathbf{I}_{3 \times 3} & (\frac{1}{2} \sigma_u^2 \Delta t^2) \mathbf{I}_{3 \times 3} \\ (\frac{1}{2} \sigma_u^2 \Delta t^2) \mathbf{I}_{3 \times 3} & (\sigma_u^2 \Delta t) \mathbf{I}_{3 \times 3} \end{bmatrix} \quad (9)$$

The second step consists of the filter update step on the basis of the measurement model. Then, let the observed measurement vector \mathbf{z}_k be given by

$$\mathbf{z}_k = \begin{bmatrix} \tilde{\mathbf{b}}_k \\ \tilde{\mathbf{s}}_k \end{bmatrix} \quad (10)$$

where $\tilde{\mathbf{b}}_k \in \mathbb{R}^3$ and $\tilde{\mathbf{s}}_k \in \mathbb{R}^3$ are vector measurements provided by the magnetometers and sun sensors, respectively, at time step k . And let the estimated measurement vector \mathbf{h}_k be given by

$$\mathbf{h}_k = \begin{bmatrix} \mathbf{A}(\hat{\mathbf{q}}_{k|k-1}) \mathbf{b}_i \\ \mathbf{A}(\hat{\mathbf{q}}_{k|k-1}) \mathbf{s}_i \end{bmatrix} \quad (11)$$

where $\mathbf{b}_i \in \mathbb{R}^3$ and $\mathbf{s}_i \in \mathbb{R}^3$ are measurement vectors provided by the IGRF 12 model and the sun position model, respectively, rotated from the inertial into the body frame by the estimated attitude matrix $\mathbf{A}(\hat{\mathbf{q}}_{k|k-1}) \in \mathbb{R}^{3 \times 3}$ at time step k . Also, we define the measurement sensitivity matrix $\mathbf{H}_k \in \mathbb{R}^{6 \times 6}$ as

$$\mathbf{H}_k \equiv \begin{bmatrix} [\mathbf{A}(\hat{\mathbf{q}}_{k|k-1}) \mathbf{b}_i \times] & \mathbf{0}_{3 \times 3} \\ [\mathbf{A}(\hat{\mathbf{q}}_{k|k-1}) \mathbf{s}_i \times] & \mathbf{0}_{3 \times 3} \end{bmatrix} \quad (12)$$

yielding the residual vector

$$\mathbf{r}_k = \mathbf{z}_k - \mathbf{h}_k \quad (13)$$

and the innovation process

$$\delta \mathbf{x} = \begin{bmatrix} \delta \boldsymbol{\theta}_k \\ \delta \boldsymbol{\beta}_k \end{bmatrix} = \mathbf{K}_k \mathbf{r}_k \quad (14)$$

The error state in (14) is composed by the attitude error described by small-angle approximation²⁴ $\delta \boldsymbol{\theta}_k \in \mathbb{R}^3$ and the bias estimate error $\delta \boldsymbol{\beta}_k \in \mathbb{R}^3$. The Kalman gain \mathbf{K}_k is obtained computing

$$\mathbf{K}_k = \mathbf{P}_{k|k-1} \mathbf{H}_k^T (\mathbf{H}_k \mathbf{P}_{k|k-1} \mathbf{H}_k^T + \mathbf{R}_k)^{-1} \quad (15)$$

where \mathbf{R}_k is the measurement covariance matrix

$$\mathbf{R}_k = \begin{bmatrix} \sigma_m^2 \mathbf{I}_{3 \times 3} & \mathbf{0}_{3 \times 3} \\ \mathbf{0}_{3 \times 3} & \sigma_{ss}^2 \mathbf{I}_{3 \times 3} \end{bmatrix} \quad (16)$$

and σ_m^2 and σ_{ss}^2 are spectral densities of the magnetometer and the sun sensor, respectively. The MEKF represents the updated attitude quaternion $\hat{\mathbf{q}}_{k|k}$ as the product of an estimated attitude quaternion $\hat{\mathbf{q}}_{k|k-1}$ and a deviation from that estimate given by^{26,27}

$$\delta \mathbf{q}_k = \frac{1}{\sqrt{1 - \|\delta \boldsymbol{\theta}_k\|^2/4}} \begin{bmatrix} 1 \\ \delta \boldsymbol{\theta}_k/2 \end{bmatrix} \quad (17)$$

The multiplicative update is computed as

$$\hat{\mathbf{q}}_{k|k} = [\delta \mathbf{q}_k \otimes] \hat{\mathbf{q}}_{k|k-1} \quad (18)$$

$$[\delta \mathbf{q} \otimes] \equiv \begin{bmatrix} \delta q_0 & -\delta \boldsymbol{\varrho} \\ \delta \boldsymbol{\varrho} & \mathbf{q}_0 \mathbf{I}_{3 \times 3} - [\delta \boldsymbol{\varrho} \times] \end{bmatrix}$$

where $\delta \boldsymbol{\varrho} = (\delta q_1, \delta q_2, \delta q_3)^T$. The updated bias is thus obtained:

$$\hat{\boldsymbol{\beta}}_{k|k} = \hat{\boldsymbol{\beta}}_{k|k-1} + \delta \boldsymbol{\beta}_k \quad (19)$$

For the covariance update equation, we consider the Joseph form equation as it is shown to be more stable and robust.²⁸ Eq. (20) guarantees that the covariance matrix is always symmetric positive definite, $\mathbf{P}_{k|k} > \mathbf{0}$, as long as the *a priori* $\mathbf{P}_{k|k-1}$ is symmetric positive definite as well.

$$\mathbf{P}_{k|k} = (\mathbf{I}_{6 \times 6} - \mathbf{K}_k \mathbf{H}_k) \mathbf{P}_{k|k-1} (\mathbf{I}_{6 \times 6} - \mathbf{K}_k \mathbf{H}_k)^T + \mathbf{K}_k \mathbf{R}_k \mathbf{K}_k^T \quad (20)$$

3.3 Calibration

The magnetic field sensors are calibrated by different calibration methods. All of them need a large set of sample data for full calibration. This set is acquired by rotating the satellite into different attitudes. The sample values should ideally be on an origin-centered sphere when plotted in 3D space. Linear and constant offsets as well as alignment cause a better approximation with an oblique ellipsoidal. We can fit the ellipsoidal on our sample data with least square methods, because our noise is Gaussian distributed. The Gaussian distribution was proven with the Shapiro-Wilk test. We calculate the obliquity of the ellipsoid by solving Wahba's Problem.¹⁹ This is done with the Singular Value Decomposition method.¹⁸ The microcontrollers apply the calibration on the raw magnetic field vector \mathbf{b}_{raw} according to formula (21). The calibrated vector is \mathbf{b}_c .

$$\mathbf{b}_c = \mathbf{R}(\mathbf{L}\mathbf{b}_{raw} - \mathbf{c}) \quad (21)$$

$\mathbf{R} \in \mathbb{R}^{3 \times 3}$ is the rotation matrix between the magnetic field sensor frames. In our calibration model it represents the obliquity of the ellipsoid. $\mathbf{c} \in \mathbb{R}^3$ is the offset vector of the ellipsoid from the center of the coordinate system. It corresponds to the offset of the magnetometer on every axis. $\mathbf{L} \in \mathbb{R}^{3 \times 3}$ is a diagonal matrix with the ratio between the main axes of the ellipsoid. It resembles the linear error of every magnetometer axis. For the offset we also use continuous and robust algorithms like Acuña's Algorithm,²⁹ which directly tries to maximize the log-likelihood of the sensor model while neglecting the change of the outer magnetic field.

The sun sensors are calibrated with the use of a turn table and a strong light source. One sensor is chosen as the reference sensor. We can then determine the alignment between the sensors by rotating it on all axes and measure the zero-crossing of the angles in the sun sensor frame. We can either apply the calibration directly on the voltage levels of the sun sensor output or on the calculated angles.

The calibration techniques are applied on ground. Sensor data can be retrieved from the satellite in space to determine the calibration parameters.

4. Attitude Control Concept

Two different control modes using only magnetic actuation are utilized for the MOVE-II mission: Detumbling and sun pointing mode. Therefore, two different control laws based on magnetic control are presented.

4.1 Detumbling Control

The detumbling controller must be able to reduce the initial angular velocities of CubeSat after ejection from its deployer. The B-dot control is a simple control law for despinning spacecrafts, which has been implemented on several CubeSat missions.^{14,15,30} This detumbling algorithm utilizes only magnetometers and magnetorquers and can despin the satellite relative to the Earth's magnetic field, since it is based on the rate of change of body-fixed magnetometer signals. The rate of change in the measured magnetic field is mainly caused by the rotation of the satellite in the Earth's magnetic field in Low Earth Orbit. Due to its established implementation in space this control law is the primary choice for the detumbling controller. The control law is given by

$$\mathbf{m}_{ctr} = -c\dot{\mathbf{b}} \quad (22)$$

where $c \in \mathbb{R}$ is a positive constant, $\dot{\mathbf{b}} \in \mathbb{R}^3$ the time derivative of the geomagnetic field and $\mathbf{m}_{ctr} \in \mathbb{R}^3$ the resulting control dipole moment. The resulting control torque is

$$\boldsymbol{\tau}_{ctrl} = \mathbf{m}_{ctrl} \times \mathbf{b} \quad (23)$$

Since it is not suitable to differentiate a noisy magnetometer signal, a filter is implemented to compute the required time derivative. This filter is realized by a linear fit routine of the GNU Scientific Library.³¹ To get a good approximation for the actual rate of change more than two magnetometer data points are considered. Therefore, a buffer module is implemented that saves a specific number of the latest measured magnetometer values.

Test Setup and Results

A Helmholtz cage is used to simulate a magnetic field vector. The Helmholtz cage is a cube of side 70 cm with two coils per axis. Each coil has 50 turns each. The coils are controlled using a software based current controller. The magnetic field of the Helmholtz coils was calibrated to compensate Earth's magnetic field. This paper presents a test result for

detumbling control, shown in Figure 9. A prototype of the satellite is suspended using a 2 m long nylon string in the center of the Helmholtz cage, so that it has one rotational degree of freedom. This setup is not ideal since the twist in the string induces a torque on the suspended satellite. This torque increases with the number of twists. The magnetic field strength is set to eight times the Earth's magnetic field. A high B-dot gain of 10000 is used. The magnetic field vector in the Helmholtz cage is rotated with a constant rotational velocity of 11 deg/s. The B-dot algorithm tries to dampen this rate of change of the magnetic field.

Figure 9 shows the results of this test. 1) Starting from a stationary satellite, the rotating field has the effect of spinning up the satellite in the same direction as the magnetic field vector. Ideally, the satellite would rotate synchronously with the cage field vector, however the aforementioned torque exerted by the string causes it to spin slower. 2) The direction of rotation of the cage field vector is reversed. At this point B-dot algorithm causes the satellite to reverse its direction of rotation. The torque from the twisted string also adds to the rotational speed. 3) The combined effect of the B-dot algorithm and the string causes the satellite to spin faster than the rotating cage field vector. In the region from 3 to 4, compensation of the difference in rotational speed by the B-dot algorithm causes the satellite's rotational speed to oscillate. 4) The direction of rotation of the cage field vector is reversed again. 5) Magnetic field vector rotation in the Helmholtz cage is stopped. This causes the satellite's angular velocity to converge to a stationary state.

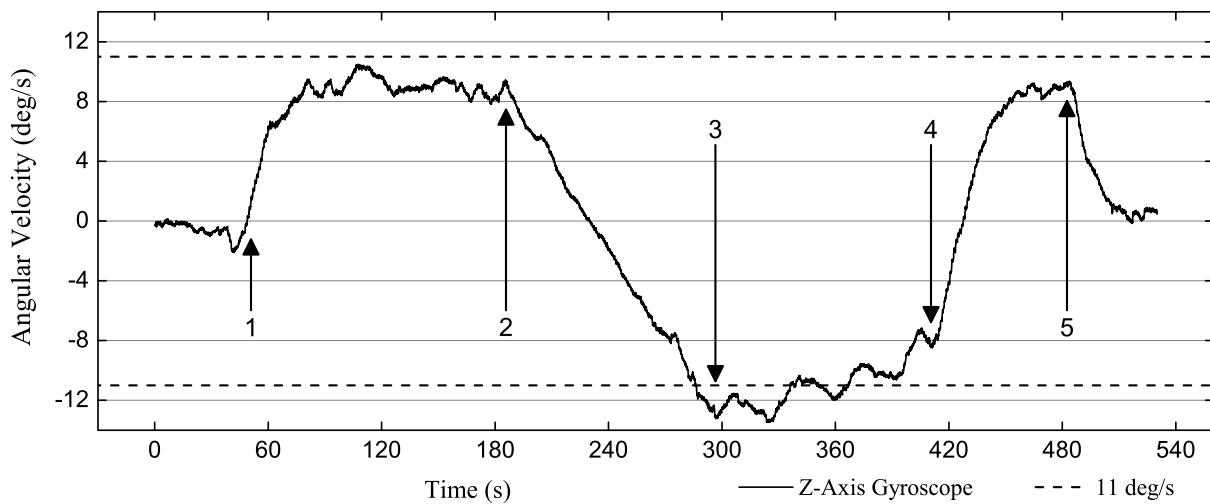


Figure 9: Angular velocity of the Mainpanel z-axis gyroscope. The magnetic field rotates with a angular velocity of 11 deg/s which is marked with the dotted line. 1) Magnetic field of the Helmholtz coil starts rotating. 2) Magnetic field rotation reversed. 3) Overshoot due to string torque. 4) Magnetic field rotation reversed again. 5) Rotation stopped with following convergence towards a stationary state.

4.2 Overview of Sun Pointing Control

For sun pointing control different approaches can be considered. We designed a linear model-based controller for the sun pointing task. Therefore, a controller that utilizes full attitude for the state feedback directly is not necessarily required, since the sun vector can be explicitly used. The terminology *reduced* attitude control shall indicate that the direction of the pointing axis and the rotation around this axis is controlled. The attitude around this axis is not specified.

In this paper only the reduced attitude control approach is presented, since it is the preferred technique for sun pointing after development investigations. Two different approaches can be distinguished: *Spin Stabilized Sun Pointing Control (SSPC)* of the satellite around the pointing axis and a non-spinning *Reduced Sun Pointing Control (RSPC)*. In the latter case the satellite points to the sun, but there is no rotation around this pointing axis. To find a stable controller gain, the control design procedure presented in Wisniewski³² used: The linear quadratic regulator (LQR) formulations exploiting the time-periodicity are well studied and Floquet theory can be utilized for stability analysis providing a powerful tool for the control design. Due to constraints in computation capacity and power supply of the ADCS a constant gain state feedback controller is chosen.

MOVE-II ADCS

The idea is to derive a linear system:

$$\delta\dot{\mathbf{x}} = \mathbf{A}\delta\mathbf{x} + \mathbf{B}\mathbf{u} \quad (24)$$

where $\delta\mathbf{x} = (s_1, s_2, \omega_1, \omega_2, \omega_3 - \omega_S)^T \in \mathbb{R}^5$ is the state vector. It consists of the components of the angular velocity ω of the satellite relative to the inertial frame (considering the spin rate $\omega_S \neq 0$ for SSPC in the last component) and the two first components of the sun vector. $\mathbf{A} \in \mathbb{R}^{5 \times 5}$ is the system matrix, $\mathbf{B} \in \mathbb{R}^{5 \times 3}$ is the control input matrix and $\mathbf{u} \in \mathbb{R}^3$ the control input vector. The control input matrix is time-periodic

$$\mathbf{B}(t) = \mathbf{B}(t + T) \quad (25)$$

with T as the system period. This is reasonable, because \mathbf{B} contains information of the magnetic field which changes approximately periodically during half an orbit. In accordance with the work of Wisniewski³² the time-periodic control input matrix has to be averaged to calculate a constant controller gain:

$$\bar{\mathbf{B}} = \frac{1}{T} \int_0^T \mathbf{B}(t) dt \quad (26)$$

The averaged control input matrix is inserted into the steady-state Ricatti equation. After finding the solution, the general state-feedback control law is given by

$$\mathbf{u} = -\mathbf{K}\delta\mathbf{x} \quad (27)$$

where $\mathbf{K} \in \mathbb{R}^{3 \times 5}$ is the constant controller gain matrix. A mapping function is used to ensure that the dipole moment is always perpendicular to the magnetic field:³²

$$\mathbf{u} \longrightarrow \mathbf{m} : \quad \mathbf{m} = \frac{\mathbf{u} \times \mathbf{b}}{\|\mathbf{b}\|} \quad (28)$$

where $\mathbf{u} \in \mathbb{R}^3$ is the new and unconstrained control input vector which can be chosen arbitrarily by the controller. Due to the mapping onto the plane perpendicular to the geomagnetic field power consumption required for actuation can be saved.³²

The advantage of this proposed control design is finding stable controller gain very easily. No further requirements and restrictions of the attitude around the pointing axis are required. This results in a simpler control problem.

Moreover, the proposed controller has the flexibility that state feedback can be obtained by two different methods: The required state vector can be either estimated by the EKF, e.g. for the required sun vector

$$\hat{\mathbf{s}} = \mathbf{A}(\hat{\mathbf{q}})\mathbf{s}_i \quad (29)$$

or measurements can be used directly for course sun pointing. In the latter case special attention has to be paid on the sun vector measurements, which are not available during eclipse and can be corrupted by albedo of the Earth.

5. Software Implementation

The ADCS software is split into two components. The ADCS subsystem daemon runs continuously on the CDH subsystem and controls the Mainpanel via SPI. The ADCS daemon provides an interface exposing the ADCS subsystem functionalities to other programs on the CDH in the form of D-Bus methods. The ADCS firmware runs on the microcontrollers of the Mainpanel, the Sidepanel and the Toppanel. The firmware exists in two versions, one for the Mainpanel and one for the Sidepanels and the Toppanel.

Both components are written in C++. C++ supports object orientated programming and abstract interfaces while still retaining low level C compatibility. Abstract interfaces reduce tight coupling between software modules. These modules are viewed as blackboxes from the outside.

In our software the modules can be of one of three types. Producers are modules gathering data from the outside world. Sensors fall into this category. Consumers are the endpoints for data, where it is used to drive the actuators in our system. The coil driver is an example for this category. Transformers are functions that get data from producers, transform it and pass the transformed data to consumers or other transformers. Additionally, a stateful transformer is allowed to keep its state between calls. For example the buffer for the magnetic field data stores previous measurements to perform a linear fit.

5.1 ADCS Operation Modes and Functionalities

The ADCS modes correspond to the different long term responsibilities of ADCS. When the data handling system of the satellite starts, ADCS is switched on in sleep mode. This mode is designed to reduce power draw while still providing a subset of sensor data to other subsystems. During Launch and Early Operation Phase (LEOP) ADCS goes into detumbling mode to execute the B-dot algorithm. After the satellite's angular speed falls below a pre-defined threshold, sun pointing mode is entered. Sun-pointing orients the Toppanel and the 4 deployed solar wings to the sun for power generation and measurement of the experimental payload cells. On the ground an additional test mode is available allowing to test and verify the system.

In addition to these modes, ADCS provides short term functionalities to other subsystems. Thermal data is provided to the Thermal subsystem and a sun vector is provided to the Payload subsystem. Housekeeping data is recorded regularly and transmitted to the ground station.

The ADCS uses input from other subsystems. TLE data support attitude determination, calibration parameters for sensors, parameters of the EKF and the controller gains can be updated.

5.2 ADCS Internal Communication

The ADCS daemon uses the main SPI bus of the satellite to send control data to the Mainpanel microcontroller and receive status and sensor data in return. To ensure the correctness of the transferred data all SPI transfers include a CRC16 checksum which is verified on the receiving side.

A direct memory access (DMA) controller allows to receive the control data asynchronously, ensuring uninterrupted execution of the algorithms running on the Mainpanel. In the next iteration of the Mainpanel processing loop the received control data is processed and the sensor and status data structure is updated. Generation counters keep track of updates to each component of the data structure. For example, when the D-Bus method to set the ADCS mode is called the daemon receives the name of the mode as a string, sets the corresponding byte in the control data structure and updates the generation counter. This data structure is then sent to the Mainpanel. When the Mainpanel detects an updated generation counter it switches to the mode set by the daemon.

Two additional SPI busses are used to transfer data from the Mainpanel to the Sidepanels (and the Toppanel). Similar to the daemon-Mainpanel interface the Mainpanel sends a control data structure and receives a sensor data structure.

5.3 Sensor Data Gathering and Processing of Algorithms

Since each panel features an independent microcontroller, we use a distributed approach for sensor data gathering and pre-processing. The measurements from the magnetometer, gyroscope and sun sensors are independently acquired on each panel. Then the resulting vectors get rotated to the central coordinate frame and corrected using adjustable calibration values. Afterwards the data from all panels is aggregated on the Mainpanel and the sun vector from the sensor with the highest light intensity is selected.

Attitude determination and control algorithms are processed centrally on the Mainpanel. The sensor data is used to calculate the attitude as described in section 3.1. Using the control algorithms described in section 4, the required magnetic control moment is calculated. As the magnetorquers influence the magnetic field measurements, time scheduling of measurement and actuation is required. While coil actuation is in progress no measurements are made and vice versa. With this approach the Sidepanel microcontrollers only act as transformers, reading and preprocessing sensor values. Additionally they control the coils on demand while sleeping the remaining time. This simplifies the design and lowers the power consumption.

5.4 Coil Actuation

In order to actuate the coils to the required control moment, the required coil current I_{ctrl} for each axis is calculated using

$$I_{ctrl} = \frac{m_{ctrl}}{NA} \quad (30)$$

where m_{ctrl} is the corresponding magnetic dipole moment value, N is the number of turns of the coil and A is the coil area. The Mainpanel then sends the I_{ctrl} value to the Sidepanels. Each panel then drives its coil and uses a timed interrupt to turn it off after the desired actuation duration. A timer counter module on the microcontroller generates the 512 kHz PWM signal required to operate the coil driver circuit. The resulting current is measured and used as a feedback signal by a proportional-integral-derivative controller that controls the pulse width of the PWM signal. The

MOVE-II ADCS

self-adjusting nature of this controller makes it independent of the coil design as well as variations in coil resistance. It is thus able to work robustly over a wide range of temperatures.

5.5 Update System

Naturally occurring space radiation produces transient and permanent changes in the electrical properties of solid-state devices and integrated circuits. This can corrupt the flash memory storing the firmware and thereby cause the system to fail. As the used Atmel microcontrollers are not radiation resistant, methods to mitigate radiation-induced degradation are required.³³ This motivated the development of a software system allowing the Mainpanel and the Sidepanel flash memory to be reprogrammed with a pristine firmware image. As an additional benefit this allows uploading new firmware with improved functionality from the ground station to the satellite in orbit. The software update of the Mainpanel microprocessor is done by flashing via CDH, the microcontrollers of the Sidepanels are flashed via the Mainpanel. Both use the PDI, an Atmel proprietary interface for external programming.¹⁰ The update system includes a program running on the CDH to flash the Mainpanel and a software module included in the Mainpanel firmware to flash the Sidepanels.

In the Linux environment on the CDH the scheduler causes the flashing program to be suspended in order to provide computing time to other processes. This interrupts the flashing process. By saving the last written address the flashing process can be resumed and the program continues writing at the saved address. The Sidepanel flashing procedure does not suffer interruptions, because the Mainpanel microcontroller is a single threaded system.

Flashing Procedure

Mainpanel updates via CDH To update the Mainpanel software, the new binary has to be uploaded to the satellite through the mission operations frontend. Then the flashing program is executed on the CDH using the ADCS daemon. The flashing software for the Mainpanel also provides the ability to erase or dump the Mainpanel flash memory to verify its integrity.

Sidepanel updates via Mainpanel The Sidepanel firmware is part of the Mainpanel firmware. When the Mainpanel receives a command to flash it writes the stored firmware to the Sidepanels. To update the Sidepanel firmware the Mainpanel has to be updated first. The new firmware contained in the Mainpanel software can then be flashed to a specific Sidepanel or several Sidepanels at once.

6. Summary, Conclusion and Outlook

This paper presents the current state of the ADCS developed for the MOVE-II CubeSat mission. The hardware was developed using an iterative prototyping process and was tested over the different project phases. The performance of actuators and sensors was characterized in different test procedures and shows promising results. During qualification tests of the MOVE-II engineering model, the ADCS hardware passed all environmental and functional requirements. Different parts of the system such as interaction with the CDH of MOVE-II have been verified successfully. In this paper also results of a detumbling test are presented.

At the time of publication we are testing the attitude estimation and sun pointing algorithm. As not all parameters of a space environment can be easily simulated, a Hardware in the Loop (HIL) test setup is being developed to verify the complete functionality of the ADCS. In this setup the ADCS hardware and software will communicate with a simulation environment developed in Matlab/Simulink to test the full interaction of control and estimation.

Based on a distributed hardware concept a partially distributed system was implemented using several low-power microcontrollers. A software update system allows to refine and extend the software to investigate on new attitude determination and control strategies. The possibility to suspend individual parts allows significant power savings while still providing the full computing capacity of six microcontrollers when needed. The described system is a good platform for future research on distributed computation on CubeSats.

7. Acknowledgments

We would like to express our thanks to all people who have supported our work in any way. We would like to thank all former members of the ADCS team for their important contribution. Furthermore, we would like to express our thanks to Prof. Huang He for taking his time for weekly research meetings and giving us advice for the ADCS development. Last but not least, our appreciation also belongs to Prof. Ulrich Walter for providing such a fruitful and open-minded

environment in which this development came into being. Finally, we would like to express our gratitude to the ESTCube team for giving us advice.

The authors also acknowledge the funding of MOVE-II by the Federal Ministry of Economics and Energy, following a decision of the German Bundestag, via the German Aerospace Center (DLR) with funding grant number 50 RM 1509.

References

- [1] H. Heidt, J. Puig-Suari, A. Moore, S. Nakasuka, and R. Twiggs. Cubesat: A new generation of picosatellite for education and industry low-cost space experimentation. 2000.
- [2] M. Dziura, M. Langer, M. Losekamm, M. Grulich, and M. Mutschler. Providing hands-on space education by involvement of collaborating self-reliant student teams.
- [3] M. Langer, N. Appel, M. Dziura, C. Fuchs, P. Günzel, J. Gutmiedl, M. Losekamm, D. Meßmann, T. Pöschl, and C. Trinitis. MOVE-II—der zweite kleinsatellit der technischen universität münchen. *Deutscher Luft-und Raumfahrtkongress (DLRK) Rostock, Germany*, 2015.
- [4] M. Czech, A. Fleischner, and U. Walter. A first-move in satellite development at the tu-münchen. In *Small Satellite Missions for Earth Observation*, pages 235–245. Springer, 2010.
- [5] M. Langer, C. Olthoff, J. Harder, C. Fuchs, M. Dziura, A. Hoehn, and U. Walter. Results and lessons learned from the cubesat mission first-move. *Small Satellite Missions for Earth Observation, Springer, Berlin*, 2015.
- [6] M. Rutzinger, L. Krempel, M. Salzberger, M. Buchner, A. Höhn, M. Kellner, K. Janzer, C. G. Zimmermann, and M. Langer. On-orbit verification of space solar cells on the cubesat move-ii. In *Photovoltaic Specialists Conference (PVSC), 2016 IEEE 43rd*, pages 2605–2609. IEEE, 2016.
- [7] M. Rossner, N. Benes, T. Grübler, S. Plamauer, and A. W. Koch. Demonstration of a Rocket-Borne Fiber-Optic Measurement System: The FOVS Experiment of REXUS 15. In *22nd ESA Symposium on European Rocket and Balloon Programmes and Related Research*, volume 730, page 415, 2015.
- [8] Atmel Corporation. Atmel-8387H-AVR-ATxmega16A4U-34A4U-64A4U-128A4U-Datasheet_092014, 2014.
- [9] Atmel Corporation. Atmel-8386E-AVR-XMEGA A3U-Datasheet_09/2014, 2014.
- [10] Atmel Corporation. Atmel-8282A-AVR1612: PDI programming driver_112010, 2010.
- [11] J. L. Crassidis and J. L. Junkins. *Optimal estimation of dynamic systems*, volume 24 of *Chapman & Hall/CRC applied mathematics & nonlinear science*. CRC Press, Boca Raton, F., 2. ed. edition, 2012.
- [12] Bosch Sensortec. Bmx055. https://ae-bst.resource.bosch.com/media/_tech/media/datasheets/BST-BMX055-DS000-02.pdf, 2014.
- [13] J. Hofman and R. Sharp. A total ionising dose, in-situ test campaign of DS18B20 temperature sensors. In *Radiation and Its Effects on Components and Systems (RADECS), 2011 12th European Conference on*, pages 871–876. IEEE, 2011.
- [14] K. Jensen and K. Vinter. *Attitude Determination and Control System for AAUSAT3*. Master thesis, Aalborg University, 2010.
- [15] P. Bangert, S. Busch, and K. Schilling. Performance characteristics of the uwe-3 miniature attitude determination and control system. In *Proceedings 2nd IAA Conference on Dynamics and Control of Space Systems, Roma*, 2014.
- [16] A. Slavinskis, H. Ehrpais, H. Kuuste, I. Sünter, J. Viru, J. Kütt, E. Kulu, and M. Noorma. Flight results of estcube-1 attitude determination system. *Journal of Aerospace Engineering*, 29(1):04015014, 2015.
- [17] P. Horowitz and W. Hill. *The Art of Electronics*. Cambridge University Press, 2015.
- [18] K. Vinther, J. K. Fuglsang, J. A. Larsen, and R. Wisniewski. Inexpensive cubesat attitude estimation using quaternions and unscented kalman filtering. *Automatic Control in Aerospace*, 4(1), 2011.
- [19] Grace Wahba. Problem 65-1: A least squares estimate of satellite attitude. *SIAM Review*, 7(3):409–409, 1965.
- [20] S. Dunlop, O. Montenbruck, R.M. West, and T. Pfleger. *Astronomy on the Personal Computer*. Springer Berlin Heidelberg, 2013.
- [21] IAGA. International Geomagnetic Reference Field. <https://www.ngdc.noaa.gov/IAGA/vmod/igrf.html>.

- [22] F. R. Hoots and R. L. Roehrich. Models for propagation of norad element sets. Technical report, DTIC Document, 1980.
- [23] S. Busch, P. Bangert, S. Dombrovski, and K. Schilling. UWE-3, in-orbit performance and lessons learned of a modular and flexible satellite bus for future pico-satellite formations. *Acta Astronautica*, 117:73–89, 2015.
- [24] J. L. Crassidis and J. L. Junkins. *Optimal Estimation of Dynamic Systems*. CRC Press, Taylor & Francis Group, 2012.
- [25] F. L. Markley and J. L. Crassidis. *Fundamentals of Spacecraft Attitude Determination and Control*. Springer, 2014.
- [26] J. L. Crassidis, F. L. Markley, and Y. Cheng. Survey of nonlinear attitude estimation methods. *Journal of Guidance, Control, and Dynamics*, 30(1):12–28, 2007.
- [27] H. L. Fisher, M. D. Shuster, and T. E. Strikwerda. Attitude determination for the star tracker mission. In *AAS/AIAA Astrodynamics Specialist Conference*, Stowe, Vermont, 1989.
- [28] P. Maybeck. *Stochastic Models, Estimation, and Control - Vol. 1*. Academic Press, 1979.
- [29] R. Alonso and M. D. Shuster. Attitude-independent magnetometer-bias determination: a survey, 2002.
- [30] T. Flatley, W. Morgenstern, A. Reth, and F. Bauer. A b-dot acquisition controller for the radarsat spacecraft. In *NASA Conference Publication*, pages 79–90. NASA, 1997.
- [31] Gnu scientific library: Least squares fitting. https://www.gnu.org/software/gsl/manual/html_node/Least-Squares-Fitting.html. Accessed: 2017-05-27.
- [32] Wisniewski, R. *Satellite Attitude Control Using Electromagnetic Actuation*. Ph.d. thesis, Aalborg University, 1996.
- [33] J. R. Srour and J. M. McGarrity. Radiation effects on microelectronics in space. *Proceedings of the IEEE*, 76(11):1443–1469, 1988.